

## GT2016-56313

Please cite: Kaiser, S., Seitz, A., Vratny, P., Hornung, M., "Unified Thermodynamic Evaluation of Radical Aero Engine Cycles", GT2016-56313, ASME Turbo Expo 2016, Seoul, South Korea, June 2016

### UNIFIED THERMODYNAMIC EVALUATION OF RADICAL AERO ENGINE CYCLES

**Sascha Kaiser**

Bauhaus Luftfahrt e.V.  
Ottobrunn, Germany

**Patrick Vratny**

Bauhaus Luftfahrt e.V.  
Ottobrunn, Germany

**Arne Seitz**

Bauhaus Luftfahrt e.V.  
Ottobrunn, Germany

**Mirko Hornung**

Bauhaus Luftfahrt e.V.  
Ottobrunn, Germany

#### ABSTRACT

The Joule-/Brayton thermodynamic cycle is the base cycle of all major contemporary aero engines. Over the decades, the achievement of further significant improvements has become progressively challenging, and the increase of efficiency approaches physical limitations. In order to meet the ambitious long-term emission reduction targets, the introduction of radical new propulsion system concepts is indispensable. Various cycles promising significant efficiency improvements over the conventional Joule-/Brayton-cycle are being examined by the engine community. However, as no clear favorite has emerged from these potential technical solutions, a transparent methodological approach for the consistent evaluation of the concepts is necessary.

Consistent thermodynamic description and performance metrics for three engine cycles are presented in this paper: The turbofan as reference and two radical engine cycles, namely the composite cycle and the cycle-integrated parallel hybrid. Laws for the estimation of component performance for large parametric variations are introduced. A method for the estimation of power plant system mass for the investigated engine cycles is proposed to evaluate fuel burn reduction. The studies substantiated that the turbofan improvement potential is saturating. The composite cycle engine offers a tremendous potential for fuel burn improvement of 24.5% over state of the art turbofan engines, which allows meeting the emission reduction targets in 2035. The cycle-integrated parallel hybrid engine improves the turbofan moderately with year 2035 technology, but is not capable of meeting the corresponding emission reduction targets on a short-to-medium range aircraft platform.

#### NOMENCLATURE

##### Symbols

$A$  Cross-sectional flow path area [m<sup>2</sup>]

$c$	Mass calibration constant [kg/(kg/s) <sup>1.5</sup> ]
$c_p$	Specific heat capacity [J/kg/K]
$CR$	Compression Ratio [-]
$d$	Piston diameter [m]
$D_{Fan}$	Fan diameter [m]
$F$	Thrust [N]
$FB$	Fuel Burn [kg]
$FAR$	Fuel-Air-Ratio [-]
$FHV$	Fuel Heating Value [J/kg]
$h$	Specific enthalpy [J/kg]
$H$	Degree of Hybridization [-]
$n$	Number of electrical components [-]
$m$	Mass [kg]
$M$	Mach number [-]
$OPR$	Overall Pressure Ratio [-]
$p$	Total pressure [Pa]
$\Delta p$	Piston engine pressure differential [Pa]
$P$	Power [W]
$\bar{P}$	Specific Power [kg/W]
$PPR$	Peak Pressure Ratio [-]
$q$	Ratio of two parameters [-]
$R$	Specific gas constant [J/kg/K]
$s$	Specific entropy [J/kg/K]
$T$	Total temperature [K]
$TSFC$	Thrust Specific Fuel Consumption [g/kN/s]
$v$	Stream velocity [m/s]
$v_{mean}$	Mean piston velocity [m/s]
$w$	Mass flow rate [kg/s]
$\bar{w}$	Non-dimensional mass flow rate [kg/s/m <sup>2</sup> ]
$WP$	Work Potential [J/kg/K]
$x$	Axial dimension of turbo component [m]
$y$	Radial dimension of turbo component [m]
$\gamma$	Heat capacity ratio [-]
$\eta$	Efficiency [-]

$\Psi$	Entropy function [-]
$\Pi$	Pressure ratio[-]
$\phi$	Cooling efficiency [-]
$\rho$	Density [ $\text{kg/m}^3$ ]

#### Acronyms

CCE	Composite Cycle Engine
CEA	Chemical Equilibrium and Applications
CIPH	Cycle-Integrated Parallel Hybrid
LHS	Latin Hypercube Sampling
LPT	Low Pressure Turbine
HPC	High Pressure Compressor
HPT	High Pressure Turbine
MTOW	Maximum Take-Off Weight
PMAD	Power Management and Distribution
SoA	State of the Art
SRIA	Strategic Research and Innovation Agenda
TO	Take-off
TOC	Top of Climb

#### Subscripts & Station Nomenclature

Bat	Battery
c	Compressor
cool	Cooling air
corr	Standard corrected
core	Core engine (from core inlet to HPT exit)
is	Isentropic
Mot	Electric motor
N	Net
p	Polytropic
pc	Piston Compressor
pe	Piston Engine
PPS	Power Plant System
Seiliger	Piston engine simulated with Seiliger cycle
std	Standard state
t	Turbine
vol	Volumetric
0	Ambient / Flight state
1D	Piston engine simulated with 1D piston model
2	Fan inlet
13	Fan bypass exit
18	Bypass nozzle exit
3	Compressor exit
34	Piston engine exit (for CCE)
35	Combustion chamber inlet (for CCE)
4	Combustion chamber exit / turbine stator inlet
41	Turbine (rotor) inlet
45	LPT inlet / core exit
5	LPT exit
8	Core nozzle exit

## INTRODUCTION

Gas turbines based on the Joule-/Brayton-cycle prevail in large, commercial transport category aircraft since the 1950s. They offer a very high weight-specific power output and reliability, and steady technological innovation has led to

significant reductions of fuel consumption over the last decades. The core efficiency of the Joule-/Brayton-cycle is constrained, however, by technical and physical boundary conditions: While in an ideal cycle representation, efficiency rises monotonically with Overall Pressure Ratio (*OPR*), in reality, optimum efficiency is subject to component efficiencies, material limitations, cooling requirements, component scaling behavior and real gas properties. Increasing *OPR* results in a decrease in High Pressure Compressor (HPC) exit flow cross-sectional area and blade height, and, thus, to higher tip losses. In addition, the HPC exit temperature increases, implying higher cooling air temperature and, thus, cooling air demand, as well as the demand for heavier and more expensive materials in the HPC and combustion chamber. Therefore, the further significant improvement of the thermodynamic efficiency of pure Joule-/Brayton-cycle based engines has become increasingly challenging [1]. In order to meet aviation's long-term environmental targets, such as a 30% lower energy demand from propulsion and power by 2035 relative to year 2000 standard according to the Strategic Research and Innovation Agenda (SRIA) [2], a paradigm shift in the introduction of advanced aero engine cycles is indispensable.

Two promising engine architectures have been examined in contrast to the contemporary Joule-/Brayton-cycle based turbofan engine: First, the Composite Cycle Engine (CCE) that combines the Joule-/Brayton-cycle with closed volume combustion in a topping cycle, implemented with piston engines [3]. Second, the Cycle-Integrated Parallel Hybrid (CIPH) engine, introducing electrical energy into the cycle by means of integrated hybrid energy propulsion systems [4], i.e. electrification of compression work.

The introduction of novel cycles requires major changes to the cycle parameters, most importantly *OPR* and combustion chamber exit temperature  $T_4$ , and imply major changes to engine size and weight. Therefore, a unified consistent thermodynamic description of the implications of the specified cycles capable of covering large parametric variations is demonstrated. Cooling air requirements, basic sizing laws and material limits are modelled appropriately to obtain meaningful sensitivities. The specified cycles are compared using important performance metrics and are benchmarked against a State of the Art (SoA) Joule-/Brayton-cycle turbofan engine. Aircraft-integrated environmental impact is minimized by optimizing fuel burn using derived trade factors.

## METHODS

The used methods allow for a comparison of different cycles in studies covering large parametric changes. This prohibits the use of detailed design methods such as flow path layout, consideration of mechanical layout and loads, or mean line turbo component design. To this end, the cycles are described with first order methods and simple descriptors capable of providing reasonable sensitivities across a wide range of parameters and reproducing the most important design aspects.

## Thermodynamics

The choice of the representation of thermodynamic fluid properties has a major impact on the level of complexity of modelling thermodynamic processes. The assumption of ideal gas properties (i.e. constant specific gas constant  $R$  and specific heat capacity  $c_p$ ) produces prohibitively large errors compared to real gas in typical gas turbine cycles: Large changes in  $c_p$  in dependence of temperature of up to 25% and in  $R$  after the combustion of fuel yield incorrect results and misleading trends in propulsion system modelling [5]. Therefore, half-ideal gas properties are assumed. In this case, the thermodynamic properties of specific heat capacity  $c_p$ , gas constant  $R$ , heat capacity ratio  $\gamma$ , enthalpy  $h$  and entropy function  $\Psi$  are functions of temperature  $T$  and Fuel-Air-Ratio  $FAR$ , but are not dependent on pressure  $p$ . The properties are derived from tabulated data based on the NASA Chemical Equilibrium and Application (CEA) database [6,7], and are used in the commercial gas turbine simulation environment GasTurb® [8] for instance.

The compression process with a pressure ratio of  $\Pi_c$  can then be modelled by the change in entropy function

$$\Psi_3 = \Psi_2 + \frac{\ln(\Pi_c)}{\eta_{p,c}} \quad (1)$$

with  $\Psi_2 = \Psi(T_2)$  and the polytropic compressor efficiency  $\eta_{p,c}$  [9]. The compressor exit temperature then results from the inverse of the entropy function with  $T_3 = \Psi^{-1}(\Psi_3)$ . As one option, the inverse function  $\Psi^{-1}$  can be obtained via iteration from the entropy function itself. With the exit temperature  $T_3$ , the power requirement of the compressor

$$P_c = w_2 \cdot (h(T_3) - h(T_2)) \quad (2)$$

can now be derived with the enthalpy  $h$ , where  $w_2$  is the mass flow through the compressor. Similarly, expansion in a turbine with an expansion pressure ratio  $\Pi_t$  and a polytropic turbine efficiency  $\eta_{p,t}$  can be modelled with

$$\Psi_5 = \Psi_4 - \ln(\Pi_t) \cdot \eta_{p,t} \quad (3)$$

Since the power requirement from the compressor  $P_c$  is given instead of the expansion ratio  $\Pi_t$ , the turbine exit temperature  $T_5$  is derived via the turbine exit enthalpy

$$h_5 = h_4 - \frac{P_c}{w_4} \quad (4)$$

where  $w_4$  is the turbine mass flow. The expansion pressure ratio  $\Pi_t$  can then be derived via equation (3).

The heat supply via isobaric combustion (as present in a conventional Joule-/Brayton-cycle) and, thus, combustor exit temperature  $T_4$  is computed with tabulated data [8] in dependence of combustor inlet temperature  $T_3$ , pressure  $p_3$  and combustor exit fuel-air-ratio  $FAR_4$  derived from NASA CEA. For isochoric combustion, as partially present in piston engine combustion, the process end temperature  $T_4$  is calculated in the

same manner as isobaric combustion assuming that the combustion products are similar. The end pressure  $p_4$  increases during isochoric combustion, and can be found using the ideal gas law

$$\frac{m_3 R_3 T_3}{p_3} = V_3 = V_4 = \frac{m_4 R_4 T_4}{p_4} \quad (5)$$

$$\begin{aligned} p_4 &= p_3 \cdot \frac{m_4}{m_3} \cdot \frac{R_4}{R_3} \cdot \frac{T_4}{T_3} \\ &= p_3 \cdot (1 + FAR_4) \cdot \frac{R_4}{R_3} \cdot \frac{T_4}{T_3} \end{aligned} \quad (6)$$

Conversion of core and bypass nozzle inlet pressures  $p_6$  and  $p_{16}$  into nozzle exit velocities  $v_8$  and  $v_{18}$  was modelled assuming ideal expansion into free stream pressure  $p_0$ . To this end, the isentropic work  $\Delta h_{is}$  (also known as Work Potential  $WP$ ) of the stream is calculated according to equations (1) and (2) with isentropic expansion (i.e.  $\eta_p = 1$ ) to ambient pressure. The nozzle exit velocity is then obtained according to Cumpsty [5] with

$$v = \sqrt{\frac{1}{2} \cdot \Delta h_{is}} \quad (7)$$

Although the bypass nozzle is usually choked at typical flight speeds, the error in computed thrust between a choked and an ideally expanding nozzle can be neglected below a nozzle pressure ratio of 3.0 [5]. The bypass nozzle exit velocity

$$v_{18} = v_0 + v_s \quad (8)$$

is prescribed by the specific bypass thrust  $v_s$ , and the core nozzle exit velocity  $v_8$  is chosen to be

$$v_8 = \frac{v_{18}}{\eta_{p,t} \cdot \eta_{p,Fan}} \quad (9)$$

to achieve optimum propulsive efficiency [5].

The piston engine cycle is represented by the Seiliger cycle, which is a blend of the ideal Otto cycle (isobaric combustion only) and the ideal Diesel cycle (isochoric combustion only). It consists of polytropic compression, partially isochoric combustion, partially isobaric combustion and polytropic expansion [10]. For cycle modelling, it was assumed in the first instance that half of the total piston engine heat  $Q_{PE}$  is added isochorically, giving the isochoric ratio

$$q_{isochoric} = \frac{Q_{isochoric}}{Q_{PE}} = 0.5 \quad (10)$$

The Seiliger cycle model was validated against a reference piston cycle simulated with a 1D piston model [3,11]. The results shown in Figure 1 for the 1D piston model (dots) show

that the first part of the combustion is indeed isochoric (solid, red line) and later crosses the isobaric line (blue, solid, broken with dots) due to simultaneous expansion and heat addition. In contrast to the Seiliger cycle representations (thick solid) with similar inlet conditions and maximum pressure, a major mismatch is produced with an error of 23% in net cycle energy between 1D piston model ( $\Delta E = 3044 \text{ J}$ ) and Seiliger model ( $\Delta E = 3730 \text{ J}$ ). The main differences are the much higher starting temperature and higher fuel-air-ratio due to imperfect scavenging considered only in the 1D cycle. Inferior scavenging is particularly relevant for 2 stroke engines, since inlet and exhaust are open at the same time. Another difference between the models is the simultaneous heat addition and expansion, resulting in a lower effective pressure.

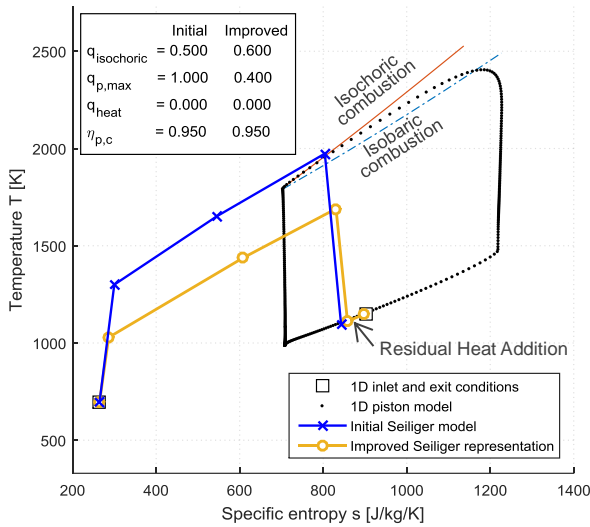


**Figure 1:** Piston cycle in a temperature over entropy diagram obtained with the 1D piston model (black dots), the initial Seiliger model (blue line, 'x' markers) and the improved Seiliger representation (orange line, 'o' markers).

In order to adapt the Seiliger representation, the cycle parameters are modified in a meaningful way to render the real cycle characteristics. The maximum Seiliger pressure

$$p_{\max, \text{Seiliger}} = p_{\max} q_{p, \max} + p_1 (1 - q_{p, \max}) \quad (11)$$

is now reduced to a value between inlet pressure  $p_1$  and maximum 1D model cycle pressure  $p_{\max}$  with the parameter  $q_{p, \max}$  to reflect the lower effective pressure during heat addition. Also, a relative heat loss

$$q_{\text{heat}} = \frac{Q_{\text{heat}}}{Q_{\text{PE}}} \quad (12)$$

during the cycle was introduced to model heat losses. It was evenly attributed to isochoric and isobaric heat addition. The model was calibrated, using the results from the 1D piston model under parametric variations of inlet temperature  $T$ , inlet

pressure  $p$ , piston diameter  $d$ , compression ratio  $CR$  and fuel air ratio  $FAR$ , giving the following results

$$\begin{aligned} q_{\text{isochoric}} &= 0.60 \\ q_{p, \max} &= 0.40 \\ q_{\text{heat}} &= 0.087 \\ \eta_{p, c} &= 95\% \end{aligned} \quad (13)$$

The heat loss parameter  $q_{\text{heat}}$  is additionally corrected depending on the input values mean piston velocity  $v_{\text{mean}}$ , compression ratio  $CR$ , inlet pressure  $p$  and temperature  $T$ , piston diameter  $d$ , Fuel-Air-Ratio  $FAR$ , and engine pressure drop  $\Delta p$ , since heat loss scales about proportionately with the mean cycle temperatures.

The Seiliger representation with the calibrated parameters from Eq. (13) yields the same work output as the 1D piston model ( $\Delta E = 3044 \text{ J}$ ) as presented in Figure 1 (orange line with circle symbols). The model has been validated against the 1D piston model with relative variations of up to  $\pm 20\%$  for each input parameter with a Latin Hypercube Sampling (LHS) plan [12]. The validation results displayed in Figure 2 show a good agreement with the 1D piston model output. The error for this region of the design space, i.e. close to the operating conditions specified in [3], is below 2.0% with a mean error of 0.09%. A variation of the input parameters in the entire parametric space being used in the study had a maximum error of 8.0% with a mean error of 0.42% (see Appendix, Figure 12).

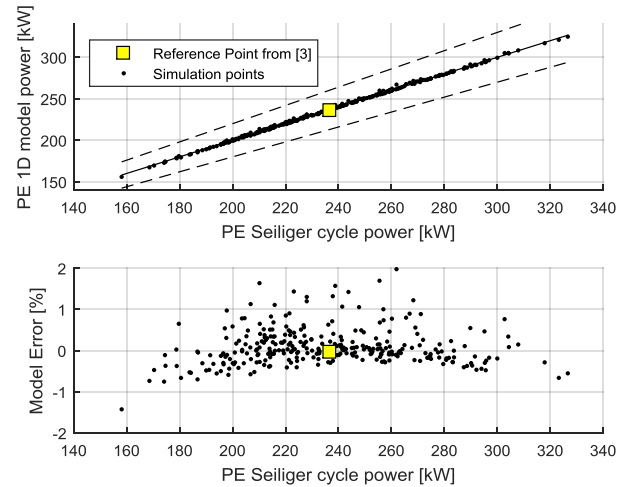


**Figure 2:** Piston engine power as obtained with 1D piston model vs. simplified Seiliger cycle (top) and error between the two (bottom) for 300 Latin hypercube sampling points.

### Component mass

The turbo component masses have been approximated using a simplified geometric representation without the resolution of individual stages. They are expressed with the standard corrected mass flow

$$w_{\text{corr}} = w \cdot \frac{\sqrt{\frac{T}{T_{\text{std}}}}}{\frac{p}{p_{\text{std}}}} \quad (14)$$

with the standard temperature  $T_{\text{std}} = 288.15$  K and pressure  $p_{\text{std}} = 101,325$  Pa. While correction with  $T_{\text{std}}$  and  $p_{\text{std}}$  is not necessary to obtain the desired scaling, it brings about the merit of having the unit as the mass flow rate. An incremental piece of a turbo component is depicted in Figure 3, showing radial and axial dimensions.

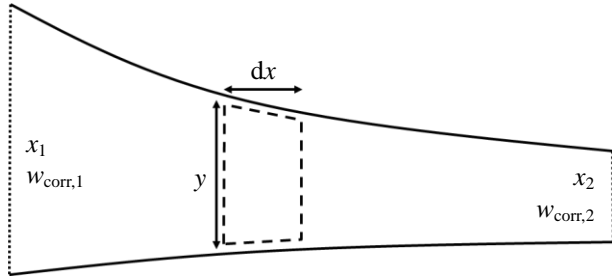


**Figure 3:** Simplified cross-section of a turbo component.

Assuming a given aspect ratio of the turbo machinery stages to begin with, the axial dimension  $x$  of a local piece of the turbo machine is proportional to the local flow path height  $y$ . Assuming further a constant axial Mach number  $M$  in the flow path, the non-dimensional mass flow rate

$$\bar{w} = \frac{w \cdot \sqrt{\frac{c_p \cdot T}{c_{p,\text{std}} \cdot T_{\text{std}}}}}{A \cdot p} = \frac{w_{\text{corr}} \cdot \sqrt{\frac{c_p}{c_{p,\text{std}}}}}{A} = f(M) \quad (15)$$

is proportional to the corrected mass flow  $w_{\text{corr}}$  divided by the cross-sectional flow path area  $A$  only, neglecting the impact of specific heat capacity  $c_p$  [5]. With a given hub-to-tip ratio, the axial dimension of the component  $x$  is then proportional to the square root of the corrected mass flow  $w_{\text{corr}}$

$$\frac{dx}{dw_{\text{corr}}} \propto \frac{1}{2 \cdot \sqrt{w_{\text{corr}}}} \quad (16)$$

The mass  $m$  of the turbo component is then obtained, assuming proportionality to the component volume

$$\begin{aligned} m &= c' \cdot \int_{x_1}^{x_2} A \, dx \\ &= c'' \cdot \int_{x_1}^{x_2} w_{\text{corr}} \, dx \end{aligned} \quad (17)$$

$$\begin{aligned} &= c''' \cdot \int_{w_{\text{corr},1}}^{w_{\text{corr},2}} \sqrt{w_{\text{corr}}} \, dw_{\text{corr}} \\ &= c \cdot |w_{\text{corr},2}^{3/2} - w_{\text{corr},1}^{3/2}| \end{aligned}$$

Appropriate calibration factors  $c$  have been determined as presented in Table 1 based on mass prediction by more sophisticated methods [13]. The factors clearly reflect the higher specific weight of high pressure turbo components due to lower axial Mach number, higher aspect ratio, higher solidity, heavier disks and use of materials with higher density.

**Table 1:** Mass calibration constants  $c$  for turbo components as specified by equation (17).

Component	Value of $c$ [kg/(kg/s) <sup>1.5</sup> ]
Fan	0.167
Intermediate Pressure Compressor	0.930
High Pressure Compressor	2.24
High Pressure Turbine	3.62
Low Pressure Turbine	0.690

The combined specific weight of the remaining bare engine components (i.e. gearbox, combustion chamber, ducts, bearings, seals, shafts, casings, accessories and mounts) was estimated with 16 kg per kN sizing thrust. The nacelle weight was estimated with 680 kg per meter fan diameter.

The piston system weight has been determined based on simple geometric representation of the piston and cylinder [3]. The specific mass flow capacity of piston components is used to determine the number of pistons required. For the piston compressor, the capacity can be expressed simply with the volumetric efficiency

$$\begin{aligned} \eta_{\text{vol}} &= \frac{w_{\text{pc}}}{w_{\text{swept}}} \\ &= \frac{w_{\text{pc}}}{\frac{\pi}{4} d^2 \cdot \frac{v_{\text{mean}}}{2} \cdot \rho_1} \end{aligned} \quad (18)$$

as defined by [10] with the swept mass flow  $w_{\text{swept}}$  representing the ideally scavenged mass flow given the inlet density  $\rho_1$  times displacement volume and frequency of the piston compressor. These are expressed by piston diameter  $d$  and the mean piston velocity  $v_{\text{mean}}$ , respectively. The volumetric efficiency of a piston compressor with a pressure ratio  $\Pi_{\text{pc}}$  of 6.0 and a compression ratio of 24 was determined to yield a volumetric efficiency of 86.0%.

The 2-stroke piston engine exhibits a different characteristic compared to the piston compressor, since it is scavenged passively through a pressure differential  $\Delta p$  between inlet and outlet. Therefore, the mass flow through the piston engine is majorly dependent on valve port area, which has been approximated by port circumference times valve lift. Therefore,

the scavenging area is proportional to the piston diameter  $d$ . In this manner, the resulting mass flow has been determined as

$$w_{pe} = 1.9 \frac{\text{kg}}{\text{s} \cdot \text{m}} \cdot d \cdot \sqrt{\frac{p_1}{p_{\text{std}}}} \cdot \sqrt{\frac{T_1}{T_{\text{std}}}} \quad (19)$$

indicating a less than proportional increase in mass flow with increasing inlet pressure  $p_1$  and reducing inlet temperature  $T_1$ . While the temperature dependency originates from the equation for corrected mass flow (14), the pressure dependency may be less than proportional due to the assumption of a constant pressure differential  $\Delta p$  across the piston. It is interesting to note that the mass flow through the piston engine has no functional dependency on the mean piston velocity  $v_{\text{mean}}$ . A more sophisticated port model may also exhibit a modified relation.

Mass of a single piston has then been obtained assuming an appropriate constant specific weight of  $0.4 \text{ g/cm}^3$  for the given piston size [14]. The cylinder mass was obtained using a simple geometric representation of cylinder and head with a wall thickness of 8 mm, nickel-based alloy as piston engine wall material and aluminum-silicon alloy as piston compressor wall material. The weight of connecting rod, crankshaft, flywheel, cylinder head accessories (such as valves), oil system and other accessories were incorporated using a scaling factor of 2.0, adapted from [3].

For the estimation of the electric component masses and efficiencies, data provided in Table 2 are used presenting a long term forecast [15]. The mass of the electrical system

$$m_{\text{Electric}} = \sum_{i=1}^n \frac{P_i}{\bar{P}_i} \quad (20)$$

is sum of the component masses obtained through individual specific power  $\bar{P}$  and power demand  $P$ . To determine the power demand, the efficiency of the entire electric component chain,  $\eta_{\text{Electric}}$ , is determined as

$$\eta_{\text{Electric}} = \prod_{i=1}^n \eta_i \quad (21)$$

**Table 2:** Overview of electric component parameters.

Component	Specific power	Mean eff. [%]
Battery [16]	-	97.0
Electric motor [17]	5 kW/kg	96.0
Controller [15]	21.0 kW/kg	99.0
Converter [15]	18.0 kW/kg	99.0
Protection switch [15]	44.0 kW/kg	99.0
Liquid cooling system [15]	1.2 kW/kg	-

\* Target of a battery system (incl. cables, housing, etc.)

The electric power demand of the battery  $P_{\text{Bat}}$  is determined by dividing the electric motor power  $P_{\text{Mot}}$  with  $\eta_{\text{Electric}}$  and adding the required cooling power  $P_{\text{cool}}$  for the electric components

$$P_{\text{Battery}} = \frac{P_{\text{Mot}}}{\eta_{\text{Electric}}} + P_{\text{cool}} \quad (22)$$

$$\text{with } P_{\text{cool}} = P_{\text{Mot}} \cdot (1 - \eta_{\text{Electric}}) \cdot 10\%$$

Previous studies have shown that the power demand of a liquid cooling system  $P_{\text{cool}}$  can be estimated to be around 10% of the rejected heat [18]. Scaling of cabling mass is neglected.

### Component scaling

The sizing impact on turbo compressor efficiency  $\eta_{p,c}$  was considered as one of the major drivers for cycle parameter choice in the investigated thrust class. To this end, a model based on corrected compressor mass flow  $w_{\text{corr}}$  was used [19], which employs a polytropic efficiency penalty for corrected mass flows below 10 lb/s (4.54 kg/s):

$$\Delta\eta_{p,c} = 0.04 \cdot \frac{\left(\frac{w_{\text{corr}}}{4.54 \text{ kg/s}}\right)^{-0.25} - 1}{0.1^{-0.25} - 1} \quad (23)$$

The relation results in an efficiency penalty of 4% at a  $w_{\text{corr}}$  of 1 lb/s. While scaling behavior is also important in turbines, the impact can be mitigated more easily by measures like adaptive clearance control.

The layout of the cooling system could only be approximated, since it is usually sized at take-off (TO) conditions, where temperature levels are highest. To this end, a simple correlation based on the mean of cooling air temperature  $T_{\text{cool}}$  (here: compressor exit temperature  $T_3$ ) and turbine entry temperature  $T_{41}$  was employed [20]. The relation has been adapted to temperature levels at top of climb to give the relative cooling mass flow

$$w_{\text{cool,rel}} = \frac{w_{\text{cool}}}{w_3} = \left(\frac{T_{\text{cool}} + T_{41}}{2} - 950 \text{ K}\right) \cdot 1 \frac{\%}{\text{K}} \quad (24)$$

A single stage turbine cooling model was considered with 62.5% of the total cooling air being introduced into the nozzle guide vane and mixed with the combustion chamber exit mass flow  $w_4$ . After the expansion according to equation (4), the remaining 37.5% of the cooling mass flow were mixed with the core mass flow. Mixing was simulated with a simple enthalpy mixer.

To validate the simplified approach for calculation of cooling air, the resulting turbine material temperature  $T_M$  was estimated. The cooling efficiency

$$\phi = \frac{T_{41} - T_M}{T_{41} - T_{\text{cool}}} \quad (25)$$

was approximated in dependency of the relative cooling mass flow  $w_{\text{cool,rel}}$  with

$$\phi = \frac{1}{\left(\frac{c_{\text{cool}}}{w_{\text{cool,rel}}}\right)^{0.735} + 1} \quad (26)$$

according to empirical data [21], where the cooling technology factor  $c_{\text{cool}}$  was chosen to be 0.032. The resulting material temperature obtained with simplified relative cooling air estimation method provides a material temperature of 1050 K ( $\pm 30$  K) for the relevant parts of the parameter space for the turbine rotor, providing a margin of 200 K for an assumed permissible material temperature of 1250 K in TO. The approach tends to underestimate cooling mass flow for combinations of very low  $T_4$  and  $OPR$  (see Appendix, Figure 13), because the cooling efficiency  $\phi$  drops close to zero, as well as for very high  $T_4$  and  $OPR$ , because the non-linearity at high cooling air demand is not adequately captured.

### Performance indicators

Engine performance has been evaluated with typical efficiency descriptors. Most importantly, the Thrust Specific Fuel Consumption

$$TSFC = \frac{w_{\text{fuel}}}{F_N} \quad (27)$$

is obtained by dividing the fuel flow  $w_{\text{fuel}}$  by the net thrust

$$F_N = v_8 w_8 + v_{18} w_{18} - v_0 w_0 \quad (28)$$

To identify the largest potential for efficiency improvement, the conversion of supplied power

$$P_{\text{supply}} = P_{\text{fuel}} + P_{\text{electric}} = w_{\text{fuel}} \cdot FHV + P_{\text{Bat}} \quad (29)$$

with the Fuel Heating Value  $FHV$  and the battery power  $P_{\text{Bat}}$  to thrust power

$$P_F = F_N \cdot v_0 \quad (30)$$

is subdivided into intermediate power metrics along the energy conversion chain [8]. The core power

$$P_{\text{core}} = w_{45} \cdot \left(\Delta h_{\text{is}} - \frac{1}{2} v_0^2\right) \quad (31)$$

is used to describe the available work potential at the core exit (when the core compressor power demand  $P_c$  is satisfied) with respect to ambient pressure  $p_0$ . The nozzle power

$$P_{\text{Nozzle}} = \frac{1}{2} \cdot (w_8 v_8^2 + w_{18} v_{18}^2 - w_0 v_0^2) \quad (32)$$

describes the increase in fluid energy from engine inlet to exit. Thus, the core efficiency

$$\eta_{\text{core}} = \frac{P_{\text{core}}}{P_{\text{supply}}} \quad (33)$$

can be used to describe the efficiency of conversion of supplied power to work potential, the transmission efficiency

$$\eta_{\text{trans}} = \frac{P_{\text{Nozzle}}}{P_{\text{core}}} \quad (34)$$

to describe conversion of core engine work potential to fluid energy, and the propulsive efficiency

$$\eta_{\text{prop}} = \frac{P_F}{P_{\text{Nozzle}}} \quad (35)$$

the conversion of fluid power to the desired thrust  $F_N$ . The combination of the three efficiencies then yields the overall engine efficiency

$$\eta_{\text{ov}} = \frac{P_F}{P_{\text{supply}}} = \eta_{\text{core}} \cdot \eta_{\text{trans}} \cdot \eta_{\text{prop}} \quad (36)$$

While  $TSFC$  is suitable to reflect the reduction in fuel need, the introduction of electrical energy is reflected adequately by  $\eta_{\text{ov}}$ .

Looking at the impact on aircraft level, a change in specific fuel consumption  $\Delta TSFC$  has cascading effects on fuel burn  $FB$ , because less fuel is required for the mission and, thus, Maximum Take-Off Weight (MTOW) reduces and the aircraft can be redesigned for the new requirements. Consequently, fuel burn  $FB$  reduces more than proportionally compared to  $TSFC$ . Likewise, increase in power plant system mass  $m_{\text{PPS}}$  increases fuel burn including impact on pylon and wing weight. Without adaptation of the sizing thrust, trade factors have been derived for small changes as follows:

$$\Delta FB_{TSFC} = 1.2 \cdot \Delta TSFC \quad (37)$$

$$\Delta FB_m = 0.004 \frac{\%}{\text{kg}} \cdot \Delta m_{\text{PPS}} \quad (38)$$

These have been determined for a typical short-to-mid range transport aircraft in an in-house aircraft simulation environment [22]. The impact of battery mass  $m_{\text{Bat}}$  has been investigated separately, because batteries are stored inside the fuselage, but no significant difference to the trade factors for power plant system weight has been found. Hence, battery mass is handled equal to power plant system mass. Cost has not been investigated quantitatively, but some implications may be drawn from the results: Changes in fuel burn implicate proportional changes in fuel cost. Engine unit cost may increase relatively more than engine weight, since engine parts with particularly expensive materials increase in weight. Unit cost has been considered qualitatively for design point selection. Maintenance cost are difficult to predict, but as a first

indication they may be assumed to increase proportionally with engine weight to reflect increase in complexity and part count.

### CYCLE SETUP AND STUDY SETTINGS

The engine application case chosen for the presented studies is a short-to-medium range aircraft with a sizing thrust of 26 kN at Top of Climb (TOC) at a flight altitude of 10,668 m (35,000 ft) and flight Mach number M0.80. The engines have been sized at TOC, which is the typical flow path sizing case for high bypass ratio engines. The respective ambient temperature  $T_0$  and pressure  $p_0$  have been calculated at International Standard Atmosphere conditions [23]. The TOC improvement in  $TSFC$  has been assumed to be representative of the average improvement throughout the mission. Although cruise provides a better indication of mission level improvements, the difference was shown to be small in previous studies [3], with 18.2% improvement at top of climb versus 17.5–18.5% in cruise for missions stage lengths between design range and a 500 nmi off-design mission. The TO case has not been calculated, assuming that enough thrust is available.

#### General

As main cycle study parameters, the burner exit temperature  $T_4$  in a range between 1300 K and 2000 K as well as Overall Pressure Ratio  $OPR = p_3/p_2$ , i.e. based on the pressure at the end of the compression process, in a range between 20 and 80 have been chosen.

The basic assumptions for component technologies are commonly shared between the cycles and are presented in Table 3. The assumptions reflect state of the art technology level. Current engines of this thrust class already provide a fuel burn improvement of 15-16% over year 2000 reference engines [24,25]. The assumptions lead to a reference turbofan as discussed in chapter ‘Cycle Simulation Results’ with good agreement with publically available data [26,27] in terms of fan diameter and engine weight, and plausible cycle parameters.

**Table 3:** Assumptions of general component parameters for a state of the art aero engine.

Variable	Unit	Value
<b>General</b>		
Fan efficiency $\eta_{p, fan}$	%	92
Compressor efficiency $\eta_{p, c}$	%	92
Turbine efficiency $\eta_{p, t}$	%	88
Combustion chamber pressure ratio	-	0.91
Bypass Pressure Ratio	-	0.97
Fuel Heating Value $FHV$	MJ/kg	42.8*
Specific bypass thrust $v_s$	m/s	95
<b>Composite Cycle Engine</b>		
Piston compression efficiency $\eta_{p, pc}$	%	95
Maximum piston pressure $p_{peak}$	MPa	10
Mean piston velocity $v_{mean}$	m/s	18
Pressure Drop $\Delta p$	kPa	100

Piston Compressor Pressure Ratio  $\Pi_{pc}$  - 6.0

#### Cycle-Integrated Parallel Hybrid

Degree of compressor hybridization  $H_c$  - 0.10

Battery specific energy kWh/kg 0.2

\*minimum fuel heating value of Jet A [28]

The turbo component efficiency for fan, compressor and turbine reflect aerodynamic conversion efficiency including mechanical shaft, bearing, and power gear box losses as well as customer offtakes. The combustion chamber pressure ratio reflects a combustion chamber pressure loss of 5% and 2% for the compressor ducts and for the turbine ducts plus nozzle, respectively. The losses were combined in the combustion chamber, assuming that the errors before and after the combustor in the center of the core engine cancel each other. The bypass pressure ratio is assumed to cater for stream tube, inlet, bypass duct and bypass nozzle losses. The specific thrust  $v_s$  has been fixed at 95 m/s to reflect the feasible fan diameter  $D_{Fan}$  for contemporary in-service aircraft. For the calculation of the fan diameter, a hub-to-tip ratio of 0.3 and an axial flow Mach number of M0.70 has been assumed.

#### Turbofan

The turbofan engine was set up as presented in Figure 4 (a) to allow for a very simple representation of the cycle. To this end, the core and bypass compression were split entirely, and the core compressor is driven by the HPT only, while the Lower Pressure Turbine (LPT) drives only the outer fan. This allows the direct calculation of core power  $P_{core}$  according to equation (31) using the states at station 45.

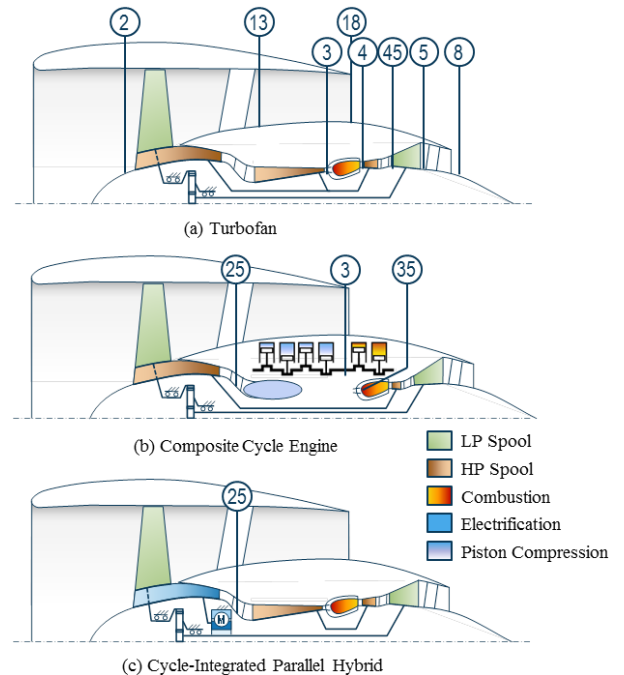


**Figure 4:** Schematic drawings with station nomenclature of the simulation setup of (a) Turbofan, (b) Composite Cycle Engine and (c) Cycle-Integrated Parallel Hybrid.

### Composite Cycle Engine

The composite cycle engine was set up as presented in Figure 4 (b) featuring a piston compressor after the core turbo compressor exit. The piston compressor is driven by a 2 stroke piston engine via a crank shaft. Cooling air is extracted at the end of the compression process at station 3. Therefore, the piston engine mass flow  $w_{pe}$  is lower than the piston compressor mass flow  $w_{pc}$ . The heat loss modelled for the piston engine is added to the cycle again after the piston engine exit between station 34 and 35, assuming that the heat is released entirely to the core mass flow. An additional pressure loss of 2% has been added to reflect losses due to additional ducting and pulsating flow caused by instationary piston operation. The piston diameter  $d$  has been fixed at 0.184 m for both piston compressors, providing a favorable compromise between piston system size and weight, and allowing for a suitable arrangement of the piston cylinders inside the core engine [3].

The peak pressure in the piston engine  $p_{peak}$  is typically reached during TO. Advanced piston technology permits a maximum pressure of about 25 MPa [10]. To this end, the peak pressure was limited to 10 MPa at design point in accordance with previous experience [3]. The pressure drop was kept constant at 100 kPa, providing a good tradeoff between losses and improved scavenging in the piston engine. The piston compressor pressure ratio  $\Pi_{pc}$  was fixed at 6.0 as a good design practice [3]. For future studies, these important parameters may be additionally investigated.

### Cycle-Integrated Parallel Hybrid

The Cycle-Integrated Parallel Hybrid (CIPH) power plant represents a special variant of a parallel hybrid power plant, where electric power is not directly supporting the power shaft, but is powering parts or the compressor as indicated in Figure 4 (c). This configuration causes a reduction of the power demand at the turbine. An important parameter describing the intensity of such a hybrid power plant design is the degree of power hybridization [29]:

$$H_p = \frac{P_{Battery}}{P_{supply}} \quad (39)$$

Previous studies [30–32] investigated various levels of  $H_p$ , indicating that optimum  $H_p$  for best performance at vehicular level strongly depends on electrical system assumptions. When considering off-design behavior, higher  $H_p$  allows for a better optimization of energy consumption in dependence of flight state [30]. However, high  $H_p$  implies challenges in matching turbomachine, electric motor and Power Management and Distribution (PMAD) in part load operation. Moreover, it infers very high battery weights, which would be well beyond the validity of the approach with trade factors and, therefore, necessitate a redesign of the entire aircraft. For easier implementation in the present studies, the degree of compressor hybridization has been defined at compressor level:

$$H_c = \frac{P_{Mot}}{P_c} = 10\% \quad (40)$$

State of the art battery systems offer a specific energy of around 200 Wh/kg (= 0.72 MJ/kg) [33]. The long term optimistic, upper bound for battery specific energy is around 1.5 kWh/kg (= 5.4 MJ/kg) [32].

## CYCLE SIMULATION RESULTS

### Turbofan

The turbofan was simulated first to identify a suitable state of the art engine cycle that serves as the reference point for the following studies. The optimum *TSFC* can be found in Figure 5 (top left) at  $T_4 = 1900$  K and  $OPR = 57$  with a *TSFC* of 14.54 g/kN/s. The changes around the optimum are, however, relatively small. It can also be seen, that the optimum is mainly driven by changes in core efficiency (Figure 5, top right). Since the specific thrust  $v_s$  is fixed, the propulsive efficiency (Figure 5, bottom left) changes little due to changes in bypass ratio. Also, the transmission efficiency (Figure 5, bottom right) stays almost constant, since low pressure component efficiencies are kept constant.

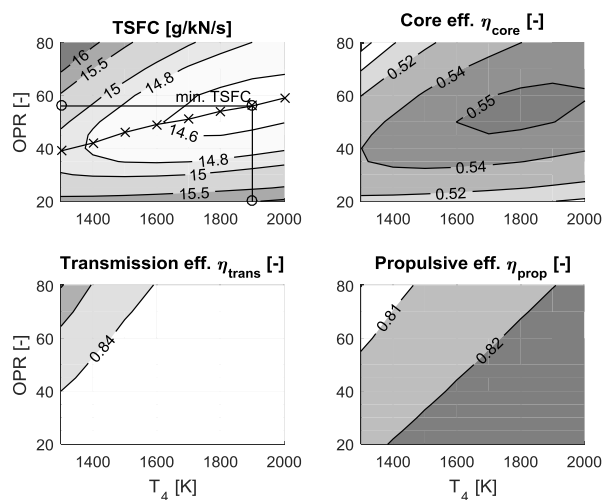


**Figure 5:** Contour plots showing optimum *TSFC* and efficiencies for combinations of  $T_4$  and  $OPR$ .

Looking at the fuel burn optima depicted in Figure 6 (left), it can be seen that they are located generally at a lower  $OPR$  than the *TSFC* optima. This effect is driven by increased turbo engine weight at higher  $OPR$ . Bypass ratio decreases towards decreasing  $T_4$  and increasing  $OPR$ , which leads to a drastic increase in compressor and HPT mass. Minimum fuel burn is obtained at  $T_4 = 2000$  K and  $OPR = 56$  (Figure 6, right). Again, the trend is very flat around the minimum. Consequently, the reference point was defined at  $T_4 = 1700$  K and  $OPR = 45$ , because the fuel burn is only 1% worse than at minimum fuel burn, while compressor complexity, cooling technology and material demands are much lower at the chosen values. The

$TSFC$  of 14.60 g/kN/s is also only 0.4% worse than optimum  $TSFC$ . It is also apparent that there is almost no margin for further fuel burn improvement from the core engine without improvements in component technology. The most important cycle parameters are summarized in Table 4.

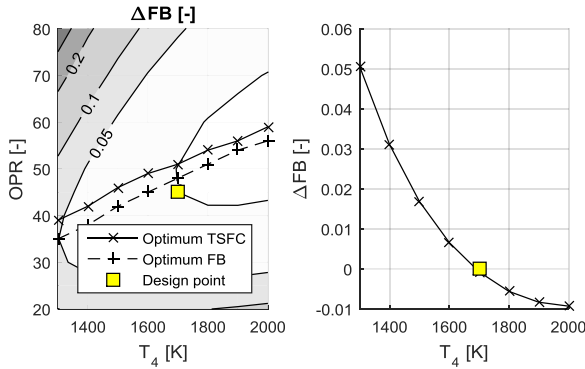


**Figure 6:** Contour plots showing optimum fuel burn  $FB$  for combinations of  $T_4$  and  $OPR$ .

**Table 4:** Summary of reference point cycle parameters for turbofan, CCE and CIPH.

Variable	Unit	Turbofan	CCE	CIPH
$T_4$	K	1700	1400	1700
$OPR$	-	45	35	45
$TSFC$	g/kN/s	14.59	12.49	13.00
$\Delta\eta_{ov}$ (rel.)	%	Ref.	+16.7	+4.9
$\Delta FB$	%	Ref.	-14.55	n/a
$m_{PPS}$	kg	3900	4700	4030
$\Pi_{Fan}$	-	1.47	1.47	1.47
$D_{Fan}$	m	2.05	2.07	2.06
$BPR$	-	13.4	20.9	15.2
$\eta_{prop}$	%	82.1	82.5	82.2
$\eta_{trans}$	%	83.5	83.7	83.4
$\eta_{core}$	%	55.0	63.5	57.6
$w_{cool,rel}$	%	22.9	8.9	23.0

### Composite Cycle Engine

For the composite cycle engine, the trends are reversed compared to the turbofan as can be seen in Figure 7. Optimum  $TSFC$  is obtained at very low  $OPR$  and  $T_4$  (Figure 7, top left).  $OPR$  levels for high efficiency are lower than for the turbofan, and they reduce with rising  $T_4$ . Although  $TSFC$  reduces monotonically with  $T_4$ , the Joule combustion chamber becomes inoperative when the piston system exit temperature  $T_{35}$  is reached at about  $T_4 = 1300$  K. These cycles have been removed from the data set and are displayed as white regions in the contour plots. Therefore, maximum permissible  $OPR$  is between 30 and 50 depending on  $T_4$  with the given cycle boundary conditions. The power plant system mass  $m_{PPS}$  reduces towards increasing  $OPR$  and  $T_4$  (Figure 7, top right), mainly driven by reduced piston system mass. The additional piston system mass is alleviated by highly reduced turbo

component masses due to reduced core mass flow  $w_{21}$  and reduced turbo compression dispensing with the HPC. The  $OPR$  for optimum  $FB$  is higher than for optimum  $TSFC$  (Figure 7, bottom left), since charging of the piston system reduces piston component sizes.

The reference point has been chosen at  $T_4 = 1400$  K and  $OPR = 35$  (cf. Table 4), in order to have enough margin in the Joule combustion chamber, so it can be switched off during cruise, while the piston system can remain at full power. This practice leads to a broad cruise bucket, allowing for very low  $TSFC$  down to 50% of sizing thrust [3], potentially resulting in even higher  $TSFC$  improvement in cruise. Power plant system mass  $m_{PPS}$  increases moderately by 800 kg. Relative cooling air  $w_{cool,rel}$  reduces drastically due to the low  $T_3$  and  $T_4$ .

In contrast to the turbofan engine, Bypass Ratio  $BPR$  increases slightly with  $OPR$  (Figure 7, bottom right). This is a direct result of the piston system taking a higher share of the core power due to higher charging, allowing for more specific work available for the fan. As an important observation, the improvement in  $TSFC$  at low  $T_4$  completely supersedes the detrimental impact of increased power plant system mass  $m_{PPS}$ . While it may be appealing to increase  $T_4$  to reduce piston system mass from a unit cost and maintenance point of view, the drawbacks due to increased  $TSFC$  are much larger.

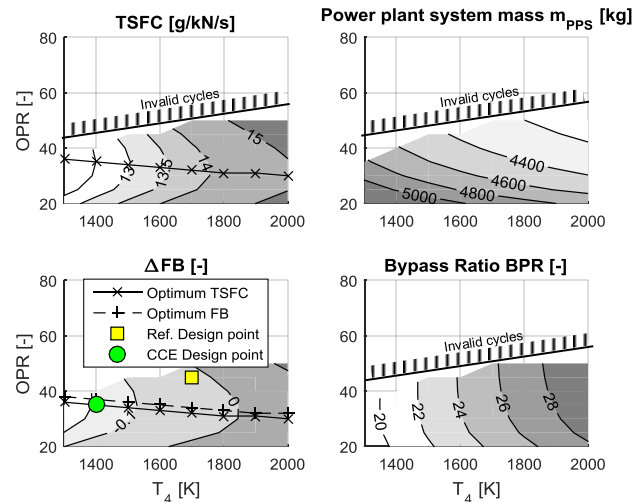


**Figure 7:** Contour plots for the CCE showing optimum  $TSFC$ ,  $m_{PPS}$ ,  $\Delta FB$  and  $BPR$  for combinations of  $T_4$  and  $OPR$ . The void areas indicate invalid cycles.

### Cycle-Integrated Parallel Hybrid

The  $TSFC$  of the CIPH improves monotonically towards lower  $T_4$  and higher  $OPR$ , as depicted in Figure 8 (left), since supplied electrical power increases and, thus, fuel flow reduces. A more meaningful metric is the overall efficiency  $\eta_{ov}$  (Figure 8, right) that reflects supplied power usage including electrical energy. Since electrical power can be utilized more efficiently than fuel, the  $OPR$  for optimum efficiency is at higher values than the turbofan. The optimum is at  $T_4 = 1700$  K and

$OPR = 63$ . Although only 10% of the compressor power  $P_c$  are electrified, the changes are significant.

While efficiency improves remarkably, battery mass  $m_{Bat}$  does increase considerably as well. The required battery mass for an assumed 3h mission is so prohibitively high that the trade factors are far from their validity range. Hence, a fuel burn assessment has been dispensed with and was only performed for the year 2035 engine. The reference point has been put to a more reasonable level of  $T_4 = 1700$  K and  $OPR = 45$  equal to the turbofan for comparison (cf. Table 4).

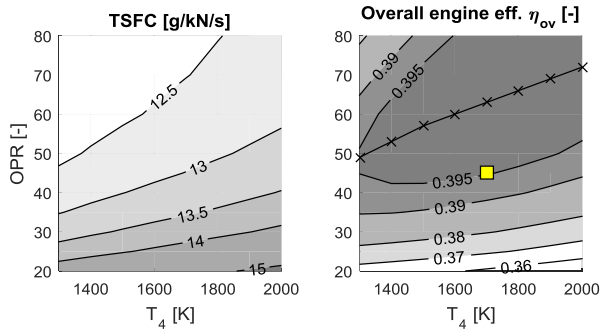


**Figure 8:** Contour plots for the CIPH showing optimum  $TSFC$ , and  $\eta_{ov}$  for combinations of  $T_4$  and  $OPR$ .

A comparison of the three engine cycles is presented in Figure 9. The turbofan and CIPH cycles are almost equal, with the HPT work of the CIPH being smaller due to reduced power requirement by the compressor. The CCE cycle provides higher specific work despite lower  $T_4$  due to a highly reduced power requirement by the turbo compressor. It may be noted that the peak temperature and pressure of the real piston engine cycle are much higher than indicated, since this only reflects the temperature level of the Seiliger cycle representation.

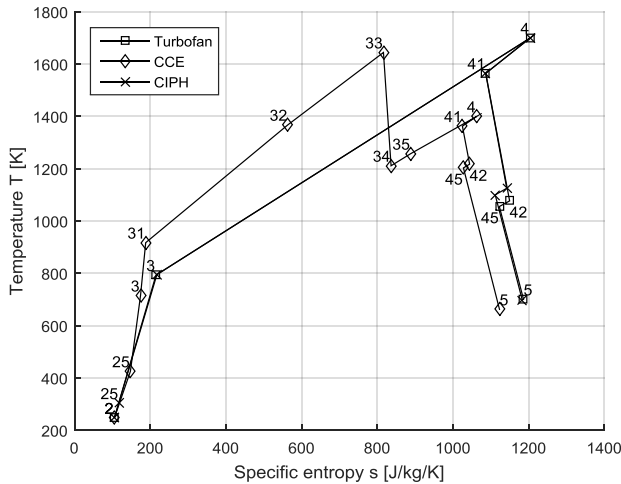


**Figure 9:** Temperature over entropy diagram comparing the engine cycles at their respective design points with station nomenclature.

### Studies at year 2035 technology level

The technology levels have been adapted to reflect expected improvements toward year 2035 to assess the applicability of the investigated engine cycles for SRIA 2035 targets. Changes in component levels have been assumed as summarized in Table 5, which may be realistically achieved with novel technologies known to date [34]. The relative changes in fuel burn due to the individual changes are displayed in Figure 10 and may be used to simulate alternative technology scenarios. The increase of turbo component efficiencies by 1% each may be achieved by improved aerodynamic design, reduced shaft and gearbox losses, and reduced customer offtakes. Specific thrust  $v_s$  reduces to 75 m/s, assuming redesigned aircraft allowing for larger fan diameter. The resulting fan diameter  $D_{Fan}$  is about 2.30 m, the fan pressure ratio  $\Pi_{Fan}$  about 1.35 and a propulsive efficiency  $\eta_{prop}$  about 85%.

Specific turbo component masses have been assumed to reduce by 10% due to increased usage of composite materials in the low temperature components and ceramics in the high temperature components. Nacelle weights have been assumed to reduce by 10% due to slim, short nacelles. The permissible material temperature has been assumed to be increased due to usage of ceramics or ceramic based composites as well as improved cooling technology. For the CCE, improvements in materials are assumed to allow for higher peak pressures  $p_{max}$  and piston acceleration, i.e. higher mean piston velocity  $v_{mean}$ . The relative changes displayed in Figure 10 indicate that the CIPH profits most from improved turbo component efficiency due to high OPR and high impact of battery weight, while the CCE profits from increased permissible material temperature through reduced cooling air demand. It can also be seen that the change in specific thrust  $v_s$  and, thus, fan diameter  $D_{Fan}$  has a minor impact of about 1%, since the reference value was already close to optimum.

**Table 5:** Assumptions of changes in component parameters for a year 2035 EIS engine.

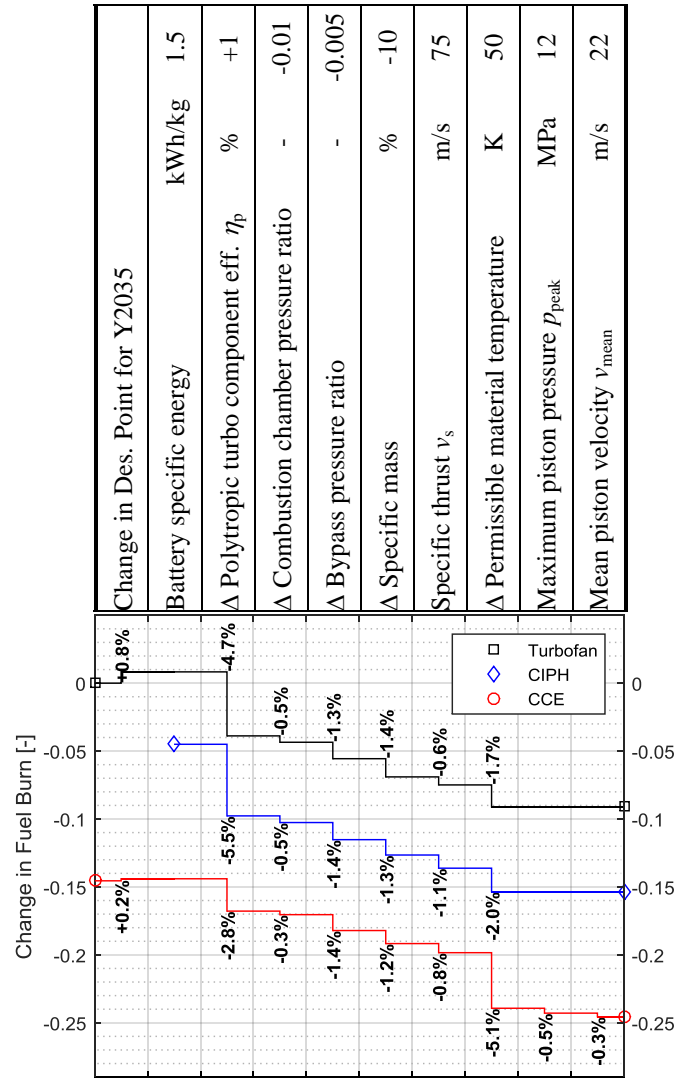


**Figure 10:** Chart of relative changes in fuel burn for each concept due to technological improvements.

The fuel burn assessment is presented in Figure 11. It can be seen that the general trends did not change compared to the state of the art cycles, with minor shifts towards increased  $OPR$ . The  $OPR$  for optimum fuel burn for the turbofan increases to slightly higher  $OPR$  (Figure 11, top left), giving a new design point at  $T_4 = 1600$  K and  $OPR = 50$  with an increase in BPR from 13.4 to 17.6. The important cycle characteristics for this design points are summarized in Table 6. Notably, combustion chamber inlet temperature decreases. The cycle parameters for minimum fuel burn are located at  $T_4 = 2000$  K and  $OPR = 63$ , but the improvement is again only 1% compared to the reference point at highly increased engine complexity. The resulting fuel burn is 9.1% lower than the reference, of which about half is accountable to improvements in turbo component efficiency. The power plant system mass

$m_{PPS}$  remains almost constant in favor of increased  $OPR$  and fan diameter  $D_{Fan}$ .

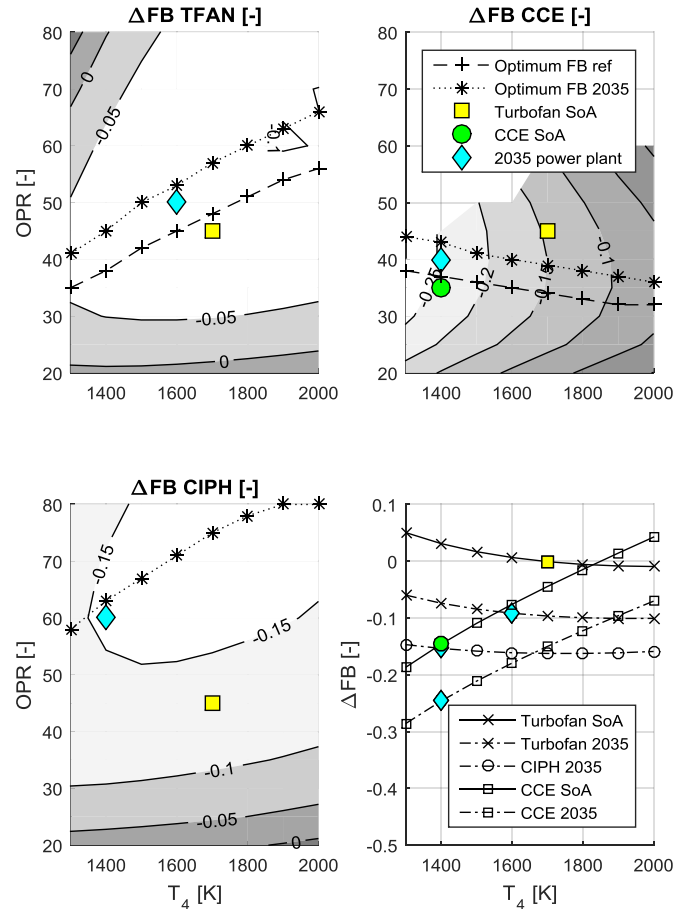


**Figure 11:** Optimum fuel burn locations for turbofan, CCE and CIPH, and comparison of fuel burn improvements against state of the art at optimum  $OPR$ .

For the CCE, the new design point is at the same  $T_4 = 1400$  K, while  $OPR$  increases from 35 to 40 (Figure 11, top right). The fuel burn improves by another 10%, to give an improvement of 24.5% against SoA. Multiplicatively combined with the improvement of state of the art engine against year 2000 technology standard of 16%, this would yield a fuel burn improvement of 36.6%. Although no improvements in specific weight for piston components were assumed, the power plant system mass  $m_{PPS}$  reduces by 230 kg.

For the CIPH power plant, fuel burn optimum was determined at very high  $OPR = 78$  and  $T_4 = 1800$  K (Figure 11, bottom left). The design point was put to  $OPR = 60$  and  $T_4 = 1400$  K, giving a fuel burn improvement of 15.3% compared to the SoA turbofan. The chosen design point has a fuel burn that is only 1% lower than optimum, while preventing excessive engine complexity to achieve very high pressure ratios. The corresponding degree of power hybridization  $H_p$  is 10.3%. The batteries contain 16,000 MJ of energy, which is equivalent to the energy content of 370 kg fuel. The power

plant including batteries weighs about 3,500 kg more than the turbofan, which is less than 10% of the MTOW for both engines. Therefore, the application of trade factors is assumed to be sufficiently accurate. While the improvements are higher than for the year 2035 turbofan, they are not sufficient to meet SRIA 2035 targets for the given mission and degree of power hybridization  $H_p$ . Thus, the CIPH architecture might need to be combined with additional technologies, such as open rotor, or be used on shorter design missions. When considering the additional power supply by the batteries, the thrust specific power consumption reduces by only 12.4%. Hence, it can be concluded that specific energy below 1.5 kW/h does not yield worthwhile improvements in power consumption for the given mission and  $H_p$ . Increasing degree of power hybridization  $H_p$  might also help to reduce carbon emissions, but this would require consideration of aircraft level impacts.

**Table 6:** Summary of reference point cycle parameters for turbofan, CCE and CIPH for year 2035 technology assumptions.

Variable	Unit	Turbofan	CCE	CIPH
$T_4$	K	1600	1400	1400
$OPR$	-	50	40	60
$TSFC$	g/kN/s	13.48	11.40	11.45
$\Delta\eta_{ov}$ (rel.)	%	+8.2	+28.0	+14.2
$\Delta FB$	%	-9.1	-24.5	-15.3
$m_{PPS}$	kg	3890	4470	4460*
$\Pi_{Fan}$	-	1.35	1.35	1.35
$D_{Fan}$	m	2.32	2.35	2.32
$BPR$	-	17.6	29.2	14.6
$\eta_{prop}$	%	85.5	85.9	85.3
$\eta_{trans}$	%	83.7	84.4	83.7
$\eta_{core}$	%	57.0	66.6	60.3
$W_{cool,rel}$	%	16.4	5.8	10.7

\* $m_{PPS} + m_{Bat} = 7420$  kg

## CONCLUSION AND OUTLOOK

A thermodynamic model for the simulation of turbofan engines, composite cycle engines and cycle-integrated parallel hybrid engine has been set up for the evaluation of performance, mass and fuel burn. A simple cycle representation model for piston engines was introduced to allow for studies of this kind. The models were used to identify favorable cycle parameters in terms of combustion chamber exit temperature  $T_4$  and overall pressure ratio  $OPR$  for each engine and to compare them against each other. For the state of the art turbofan engine, a cycle has been defined at  $T_4 = 1700$  K and  $OPR = 45$ , which provided a compromise between optimum fuel burn and engine complexity, and served as the reference for all following assessments. For the composite cycle engine, an improvement potential of 15% exists with state of the art technology. Optimum operating conditions are at a very low  $T_4$  of 1400 K and a medium  $OPR$  of 35. The cycle-integrated parallel hybrid engine exhibited optimum efficiency for very high  $OPR$  between 50 and 70, but fuel burn was not assessed due to

excessive battery mass with state of the art battery energy density.

Furthermore, the engines were compared with technology assumed for the year 2035 to investigate applicability to future emission reduction targets. The turbofan engine was shown to improve by 9% at increased  $OPR = 50$ . It could be shown that  $T_4$  does not increase for a balanced design point. The optimum composite cycle engine also shift towards higher  $OPR$ , giving an optimum design at  $OPR = 40$  and  $T_4 = 1400$  K. As an important outcome, advanced technologies do not diminish the 15% fuel burn advantage against Joule-/Brayton-cycle based turbofan engines. Moreover, the fuel burn improvement over state of the art engines of 24.5% yields a multiplicatively combined fuel burn improvement of 36.6% against year 2000 technology standard, widely exceeding the SRIA 2035 targets of reducing power plant energy demand by 30%. Therefore, this cycle is also a promising candidate for reaching SRIA 2050 targets. The cycle-integrated parallel hybrid engine design point is at an  $OPR$  of 60 with very low  $T_4 = 1400$  K with a fuel burn improvement of 15% and a 12% reduction in power consumption. While this concept may yield minor improvements in inflight  $CO_2$  emissions, it is not suitable to meet SRIA 2035 targets for the given application case and design mission of 3h (~1500 nmi), but may be used for shorter mission lengths or with a redesigned aircraft allowing for higher degrees of hybridization. All concepts show considerable improvements at low combustion chamber exit temperatures between 1400 K and 1600 K, which shows that efficiency improvements do not need to be tied to an increase in  $T_4$ .

For the studies of the future radical cycles, the additional variation of cycle parameters, especially piston compressor pressure ratio  $\Pi_{pc}$  and piston pressure drop  $\Delta p$  for the composite cycle engine as well as the power hybridization ratio  $H_p$  for the CIPH are desirable. Application to short range or long range aircraft may have an impact on the design decisions. Consideration of off-design scenarios, especially take-off and cruise is advisable to improve confidence in optimum cycle choice and mission improvement potential, and to take respect of additional component limits.

The analysis of further radical turbo engine cycles is warranted to incorporate comprehensive assessment of further technologies and their prospects of meeting future emission reduction targets. In this context, the evaluation of sequential combustion as a cycle similar to the composite cycle engine, and introduction of intercoolers and recuperators is needed.

## REFERENCES

- [1] Kurzke, J., 2003, "Achieving Maximum Thermal Efficiency with the Simple Gas Turbine Cycle," Proc. Ninth CEAS Eur. Propuls. Forum Virtual Engine—A Chall. Integr. Comput. Model.

- [2] Advisory Council for Aviation Research and innovation in Europe (ACARE), 2012, Realising Europe's Vision for Aviation - Strategic Research & Innovation Agenda - Volume 1.
- [3] Kaiser, S., Donnerhack, S., Lundbladh, A., and Seitz, A., 2015, "A Composite Cycle Engine Concept with Hecto-Pressure Ratio," 51st AIAA/SAE/ASEE Joint Propulsion Conference, Orlando, FL.
- [4] Schmitz, O., and Hornung, M., 2013, "Unified Applicable Propulsion System Performance Metrics," J. Eng. Gas Turbines Power, **135**(11), p. 111201.
- [5] Cumpsty, N., 1993, Jet Propulsion - A Simple Guide to the Aerodynamic and Thermodynamic Design and Performance of Jet Engines, Cambridge University Press, Cambridge.
- [6] Gordon, S., and McBride, B. J., 1994, Computer Program for Calculation of Complex Chemical Equilibrium Compositions and Applications - Part I: Analysis, Cleveland, Ohio.
- [7] McBride, B. J., and Gordon, S., 1996, Computer Program for Calculation of Complex Chemical Equilibrium Compositions and Applications - Part II: User Manual and Program Description, Cleveland, Ohio.
- [8] Kurzke, J., 2007, "GasTurb 11 - Design and Off-Design Performance of Gas Turbines."
- [9] Kurzke, J., 2007, "GasTurb Details 5 - An Utility for GasTurb 11."
- [10] Merker, G. P., and Teichmann, R., 2014, Grundlagen Verbrennungsmotoren, Springer Fachmedien Wiesbaden, Wiesbaden.
- [11] VanGerpen, J. H., 1990, A Two-Stroke Diesel Engine Simulation Program, Ames, Iowa.
- [12] McKay, M. D., Beckman, R. J., and Conover, W. J., 1979, "Comparison of three methods for selecting values of input variables in the analysis of output from a computer code," Technometrics, **21**(2), pp. 239–245.
- [13] Seitz, A., 2012, "Advanced Methods for Propulsion System Integration in Aircraft Conceptual Design," Technischen Universität München.
- [14] Köhler, E., and Flierl, R., 2009, Verbrennungsmotoren - Motormechanik, Berechnung und Auslegung des Hubkolbenmotors, Vieweg+Teubner | GWV Fachverlage GmbH, Wiesbaden.
- [15] Isikveren, A. T., Seitz, A., Vratny, P. C., Pernet, C., Plötner, K. O., and Hornung, M., 2012, "Conceptual Studies of Universally- Electric Systems Architectures Suitable for Transport Aircraft," Deutscher Luft- und Raumfahrt Kongress 2012, Berlin, Germany, DLRK, Berlin, Germany.
- [16] Kuhn, H., and Sizmann, A., 2012, "Fundamental Prerequisites for Electric Flying," Deutscher Luft- und Raumfahrt Kongress 2012, Berlin, Germany, DGLR, Berlin, pp. 1–8.
- [17] Siemens, 2013, Flying with Siemens Integrated Drive System, Nuremberg.
- [18] Vratny, P. C., Kuhn, H., and Hornung, M., 2015, "Influences of Voltage Variations on Electric Power Architectures for Hybrid Energy Aircraft," Deutscher Luft- und Raumfahrtkongress 2015, DGLR, Rostock, Germany.
- [19] Glassman, A. J., 1992, Users Manual for Updated Computer Code for Axial-Flow Compressor Conceptual Design, Toledo, Ohio.
- [20] Grieb, H., 2004, Projektierung von Turboflugtriebwerken, Birkhäuser Verlag, Basel-Boston-Berlin.
- [21] Livingood, J. N. B., Ellerbrock, H. H., and Kaufman, A., 1971, Nasa Turbine Cooling Research Status Report, Cleveland, Ohio.
- [22] Pace GmbH, 2011, "PACE - Pacelab APD."
- [23] International Civil Aviation Organization, 1993, Manual of the ICAO Standard Atmosphere Extended to 80 Kilometres.
- [24] Pratt & Whitney, 2015, "PW1100G-JM Engine" [Online]. Available: [https://www.pw.utc.com/Content/Press\\_Kits/pdf/ce\\_pw\\_1100g\\_pCard.pdf](https://www.pw.utc.com/Content/Press_Kits/pdf/ce_pw_1100g_pCard.pdf). [Accessed: 19-Nov-2015].
- [25] CFM International, 2015, "LEAP - The Power of the Future" [Online]. Available: <http://www.cfmaeroengines.com/files/brochures/LEAP-Brochure-2015.pdf>. [Accessed: 19-Nov-2015].

- [26] European Aviation Safety Agency (EASA), 2015, Type-Certificate Data Sheet for PW1100G-JM Series Engines.
- [27] European Aviation Safety Agency (EASA), 2015, Type-Certificate Data Sheet for LEAP-1A & LEAP-1C series engines.
- [28] Coordinating Research Council, 1983, Aviation Fuel Properties, Atlanta, Georgia.
- [29] Lorenz, L., Seitz, A., Kuhn, H., and Sizmann, A., 2013, "Hybrid Power Trains for Future Mobility," Dtsch. Luft- und Raumfahrt Kongress 2013.
- [30] Vratny, P. C., Kaiser, S., Seitz, A., and Donnerhack, S., 2016, "Performance Investigation of Cycle-Integrated Parallel Hybrid Turboshafths," Proceedings of the ASME Turbo Expo 2016, ASME, Seoul, South Korea.
- [31] Seitz, A., and Hornung, M., 2015, "Pre-Concept Investigation of Hybrid- and Full-Electric Aero Propulsion," NATO Applied Vehicle Technology 2015.
- [32] Pornet, C., Kaiser, S., Isikveren, A. T., and Hornung, M., 2014, "Integrated Fuel-Battery Hybrid for a Narrow-Body Sized Transport Aircraft," Aircr. Eng. Aerosp. Technol. J., **86**(5).
- [33] Christensen, J., Albertus, P., Sanchez-Carrera, R. S., Lohmann, T., Kozinsky, B., Liedtke, R., Ahmed, J., and Kojic, A., 2012, "A Critical Review of Li/Air Batteries," J. Electrochem. Soc., **159**(2), p. R1.
- [34] Aerospace Systems Design Laboratory (ASDL) Georgia Institute of Technology, 2009, IATA Technology Roadmap - Technical Annex.

## ANNEX A

### COMPLEMENTARY FIGURES

The annex contains complementary figures for better understanding of the material provided in the main text.

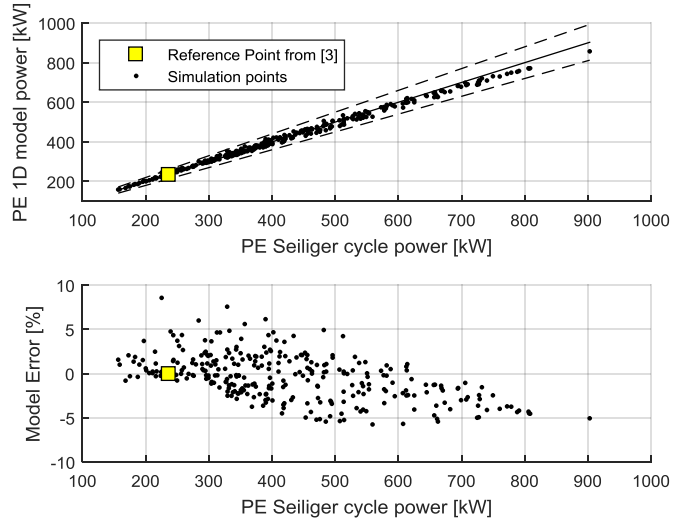


**Figure 12:** Piston engine power as obtained with 1-D piston model vs. simplified Seiliger cycle (top) and error between the two (bottom).

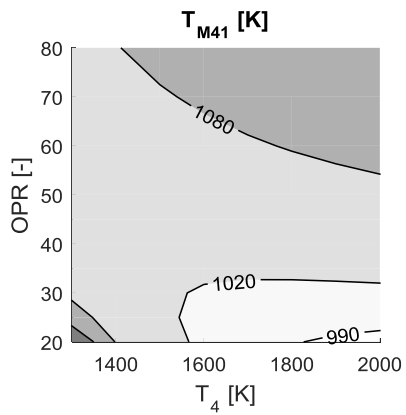


**Figure 13:** Material temperatures obtained when using the simple cooling air estimation provided in equation (24).